buildings

MDPI

Article

Optimization of Mechanical Properties and Shrinkage Resistance of Ternary-Hybrid-Fiber-Reinforced Geopolymer Concrete Using Simplex-Centroid Design

Zhenyv Liu [1], Xiliang Ning [1], Long Li [2], Yuanyuan Li [1,*], Jiahui Jin [3], Jianfeng Li [4], Ruiyang Sun [1] and Tracey Ilunga wa Ngoy [1]

[1] School of Civil Engineering and Architecture, Northeast Electric Power University, Jilin 132012, China; 2202300980@neepu.edu.cn (Z.L.); ningxiliang@neepu.edu.cn (X.N.); 2202501060@neepu.edu.cn (R.S.); 2202480009@neepu.edu.cn (T.I.w.N.)
[2] Public Education Department, Jiujiang Polytechnic University of Science and Technology, Jiujiang 332020, China; lixiaolong2008com@163.com
[3] Dalian Power Genesis Design Co., Ltd., Dalian 116023, China; jinjiahui@china-hei.com
[4] CGN New Energy Holdings Co., Ltd., Harbin 150090, China; ljfone1005@163.com
* Correspondence: 20243270@neepu.edu.cn

Abstract

The engineering application of geopolymer concrete (GPC) faces significant challenges due to its brittleness and high shrinkage. This study employs a simplex-centroid design to develop quantitative predictive models and regression equations for the multi-objective optimization of fiber hybridization in GPC. These models correlate fiber combinations with performance responses to systematically investigate the effects of steel fiber (SF), polypropylene fiber (PF), and basalt fiber (BF) incorporation on the mechanical properties and early-age shrinkage of the composite. The results indicate that binary hybrid systems, particularly SF-PF, exhibit strong synergy. Specimen GPS0.4P0.1 demonstrates a 36.8% increase in compressive strength and a 77.3% enhancement in flexural strength. For ternary hybrids, medium and high SF dosages provide the greatest improvement in mechanical performance. Furthermore, incorporating fibers effectively reduces early-age shrinkage. The BF-PF binary system was most effective in inhibiting shrinkage. Specimen GPB0.25P0.25 indicates a remarkable reduction in shrinkage, achieving a decrease of 90.9%. An optimal proportion range for ternary hybrid fibers was identified. SEM analysis revealed that crack-resistance mechanisms are stage-specific to fibers within the GPC matrix.

Keywords: geopolymer concrete; hybrid fibers; simplex-centroid method; flexural toughness; early-age shrinkage

check for updates

Academic Editor: Cedric Payan

Received: 29 September 2025
Revised: 24 October 2025
Accepted: 25 October 2025
Published: 28 October 2025

Citation: Liu, Z.; Ning, X.; Li, L.; Li, Y.; Jin, J.; Li, J.; Sun, R.; Ilunga wa Ngoy, T. Optimization of Mechanical Properties and Shrinkage Resistance of Ternary-Hybrid-Fiber-Reinforced Geopolymer Concrete Using Simplex-Centroid Design. *Buildings* **2025**, *15*, 3901. https://doi.org/10.3390/buildings15213901

Copyright: © 2025 by the authors. Licensee MDPI, Basel, Switzerland. This article is an open access article distributed under the terms and conditions of the Creative Commons Attribution (CC BY) license (https://creativecommons.org/licenses/by/4.0/).

1. Introduction

With the rapid advancement of global urbanization, cement concrete—the most widely used construction material—has raised significant environmental concerns due to its production processes. Statistics indicate that the production of 1.0 tons of ordinary Portland cement emits 0.6–1.0 tons of CO_2 [1], with the cement industry contributing approximately 8% of global anthropogenic carbon emissions [2]. As the world's largest cement producer, China produced 2.38 billion tons of cement in 2021, which accounted for approximately 13% of the nation's total carbon emissions [3]. Under the constraints of the "dual carbon" goals (carbon peak and carbon neutrality), the development of low-carbon cementitious

materials has emerged as a critical research direction in the field of construction materials [4]. By utilizing industrial solid wastes (e.g., fly ash (FA) and slag (SL)) as raw materials and using a unique "alkali-activated" reaction mechanism [5], geopolymer concrete (GPC) can completely replace traditional cement. Turner et al. [6] reported that CO_2 emissions are reduced by more than 80% in the GPC production process compared to conventional methods, establishing GPC as one of the most promising green construction materials endorsed by contemporary research [7].

The formation of geopolymers relies on the depolymerization–reorganization process of alumino-silicate precursors within a highly alkaline environment [8]. Previous studies have demonstrated [9,10] a synergistic effect when combining fly ash and slag in a fly ash–slag (FA-SL) composite system. Specifically, fly ash serves as a stable source of silicon and aluminum, while the calcium oxide content in slag accelerates reaction kinetics and enhances early-age strength. Regarding activator selection, a composite solution of sodium hydroxide and sodium silicate, characterized by moderate alkalinity and excellent dissolution properties, effectively promotes the depolymerization of precursors and facilitates the formation of a dense sodium aluminosilicate hydrate (N-A-S-H) gel network [11,12]. By optimizing precursor ratios and adjusting the activator modulus (SiO_2/Na_2O ratio), researchers have successfully developed high-performance GPC. Abdellatief et al. [13] achieved a 28-day compressive strength of 80 MPa, demonstrating the potential of GPC to replace conventional concrete in structural engineering applications [14].

However, in-depth studies have revealed significant limitations that hinder the engineering application of GPC. Similar to conventional concrete, GPC exhibits pronounced brittleness. Maganty et al. [15] found that the fracture energy of GPC is only 60–70% of that of ordinary Portland cement concrete (OPCC), and its flexural strength is generally lower than that of cementitious materials of the same strength grade [16,17]. More critically, Wallah et al. [18] documented that ambient-cured GPC exhibits a drying shrinkage of up to 1500 με, which is 2–3 times higher than that of OPCC. This phenomenon is primarily attributed to the denser Al-O-Si gel network in GPC, which exacerbates autogenous shrinkage [19]. Li et al. [20] demonstrated that when dried at a relative humidity of 50%, early-age GPC specimens, cured for one day, developed obvious surface macrocracks after 28 days, while OPCC exhibited no visible cracks even after 90 days. Stress measurements revealed that the shrinkage stress generated in GPC during the initial drying phase exceeded that of OPCC by more than threefold. Furthermore, Bernal et al. [21] found that when the crack widths in GPC surpassed 150 μm, the attack rate of sodium sulfate solutions increased to 2.3 times that of OPCC under identical exposure conditions. Addressing these brittleness characteristics and controlling contraction cracking has become a critical technical bottleneck for the practical application of GPC.

To address these challenges, researchers have explored various improvement strategies. Duan et al. [22] demonstrated that incorporating 5% nano-TiO_2 into GPC reduced the shrinkage value by 50%. However, this modification resulted in a substantial increase in material costs. Zhang et al. [23] showed that the incorporation of superabsorbent polymers (SAPs) achieved a 60% reduction in the 28-day shrinkage value. Nevertheless, this method accelerated the hydration kinetics, leading to a 40–50% reduction in the interval between initial and final setting times. The microbial mineralization method proposed by Zhang et al. [24] can form $CaCO_3$ repair bodies within cracks, while their experimental results necessitated strict initial crack width constraints (<0.09 mm). Meanwhile, Hosseinzadehfard and Mobaraki [25] investigated a new concrete mortar designed to enhance the mechanical and corrosion resistance of structures [26]. Although these approaches yielded partial improvements, they are generally limited by high costs, complex processes, or restricted applicability. In contrast, fiber reinforcement technology has emerged as the most

promising solution due to its cost-effectiveness, ease of implementation, and significant potential for performance enhancement [27–29].

The development of fiber-reinforced concrete (FRC) technology over several decades has established a comprehensive theoretical framework [30]. The incorporation of SF alone can enhance the fracture energy of concrete by 3–5 times; however, the associated high density and susceptibility to corrosion limit application in wet environments [15,31]. Polypropylene fibers are effective in bridging cracks during the plastic stage to reduce shrinkage, but also demonstrate limited capacity for strength enhancement [32,33]. As eco-friendly mineral reinforcements, Basalt fibers exhibit strong corrosion resistance and favorable interfacial bonding with geopolymer matrices [34]. However, Xu et al. [35] reported that excessive incorporation of BF (greater than 0.3 vol%) significantly deteriorates workability, primarily due to fiber agglomeration and increased porosity within the composite. Notably, hybrid-fiber technology leverages the synergistic effects of multiscale fibers to optimize performance across different stages of concrete behavior: microfibers mitigate early plastic shrinkage, while macro fibers prevent macroscopic crack propagation [36]. Sukontasukkul et al. [37] investigated the effect of blending SFs and PFs on the flexural performance of geopolymer concrete. Their results demonstrated that the hybrid combination enhanced the flexural strength, toughness, and residual strength of polypropylene fiber-reinforced geopolymer concrete (PFGPC) to varying degrees. However, mixing different fiber combinations may induce beneficial "positive hybrid effects" as well as adverse "negative hybrid effects" that compromise various concrete properties [38]. Therefore, systematic investigations into the performance and practical applications of hybrid-fiber-reinforced geopolymer concrete (HFRGPC) are critical for advancing real-world adoption.

Although fiber-reinforced geopolymer concrete has shown promise, the current understanding of hybrid-fiber systems remains incomplete. Existing research has predominantly focused on cement-based materials, while the synergistic mechanisms and optimization design strategies of multiscale fibers in GPC have been less explored. In particular, there is a lack of systematic investigation into the quantitative relationships between fiber types, dosages, and key properties such as mechanical strength, toughness, and early shrinkage. To address this, the present study employs a simplex-centroid design to systematically optimize a ternary hybrid system comprising steel fiber, polypropylene fiber, and basalt fiber in GPC. By developing high-precision regression models, quantitative predictions of key performance indicators (including mechanical strength, toughness, and early shrinkage) were achieved.

Furthermore, through correlative analysis of macro-properties and microstructural characteristics, the stage-specific synergistic toughening mechanisms of multiscale fibers during concrete cracking were elucidated. Concurrently, it was revealed that the binary fiber system achieves an ultra-high early-age shrinkage reduction rate in GPC via a "rigid–flexible composite restraint" mechanism. The findings of this study provide a theoretical basis for the design of high-performance, low-shrinkage GPC, thereby promoting its engineering application and offering material-level solutions to support the national "dual carbon" goals.

2. Experimental Program

2.1. Materials

SL (Grade S95) and Class F (low-calcium) FA were utilized as precursors in the present study; their chemical compositions are presented in Table 1.

Table 1. Chemical composition of FA and SL (wt.%).

Composition	SiO_2	Al_2O_3	Fe_2O_3	CaO	Na_2O	MgO	K_2O	SO_3
FA	62.04	25.50	4.28	4.01	0.46	1.27	2.04	—
SL	34.50	15.35	0.83	35.99	—	6.58	0.62	2.50

Note: FA represents fly ash, and SL represents slag.

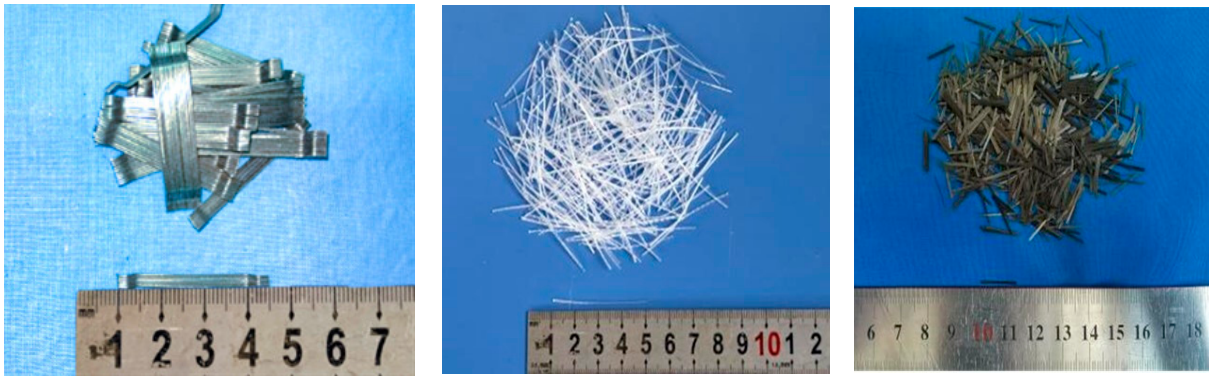
The fine aggregate was river sand, which had a fineness modulus of 2.49 and was identified as Zone II medium sand through sieve analysis. The coarse aggregate was graded crushed stone, which had a specific mass of 2530 kg/m^3 and particle sizes of 5~15 mm.

The composite alkali activator was synthesized by blending sodium silicate solution (Type B water glass, with a modulus of 3.29) with reagent-grade sodium hydroxide solids (98.0% purity).

Three types of fibers were tested: hooked-end SF, chopped BF, and textile-grade PF. The key performance parameters of these fibers are summarized in Table 2, and their morphological characteristics are illustrated in Figure 1.

Table 2. Properties of different fibers.

Fiber Type	Length (mm)	Equivalent Diameter (mm)	Density (g/cm^3)	Tensile Strength (MPa)	Elastic Modulus (GPa)
Hooked-end SF	35	0.75	7.85	1100	200
Textile-grade PF	40	0.22	0.92	650	5
Chopped BF	12	0.0165	2.66	1140	93.1



(**a**) (**b**) (**c**)

Figure 1. Various fiber types: (**a**) hooked-end SF; (**b**) textile-grade PF; (**c**) chopped BF.

Based on the GPC mix design methodology proposed by Li et al. [39], this study formulated the basic GPC mix proportions by adjusting the sand ratio, sodium silicate modulus, and alkali-activator-to-binder ratio, with a comprehensive evaluation of their effects on concrete mechanical performance and workability. The finalized mix proportions are presented in Table 3.

Table 3. GPC mix proportions (kg/m^3).

SL	FA	Sand	Coarse Aggregate	Sodium Silicate Solution	NaOH	Water
400	100	660	1077	151.8	21.6	96.7

2.2. Specimen Preparation

The simplex-centroid design, developed for experiments involving multiple mixture variables, was introduced by Scheffe in 1963 [40]. This design enables the establishment of regression equations and contour plots with high fitting accuracy, predictive capability, and precision between dependent and independent variables. Previous studies have demonstrated its advantages, which include high accuracy, strong reliability, and fewer experimental runs being required [41,42]. Therefore, this study employs a total dosage constraint of 0.5% by volume. Based on simplex-centroid theory, 13 distinct mixture proportions with varying fiber volume fractions were formulated, as illustrated in Figure 2 and detailed in Table 4. The concrete performance was expressed through the volumetric fraction of each component, as defined in Equation (1):

$$y_i(x_1, x_2, x_3) = \beta_1 x_1 + \beta_2 x_2 + \beta_3 x_3 + \beta_1\beta_2 x_1 x_2 + \beta_1\beta_3 x_1 x_3 + \beta_2\beta_3 x_2 x_3 + \beta_1\beta_2\beta_3 x_1 x_2 x_3 \quad (1)$$

where y_i is the performance of concrete, β_i is the regression model coefficient, and x_i is the volume fraction of each component (vol.%).

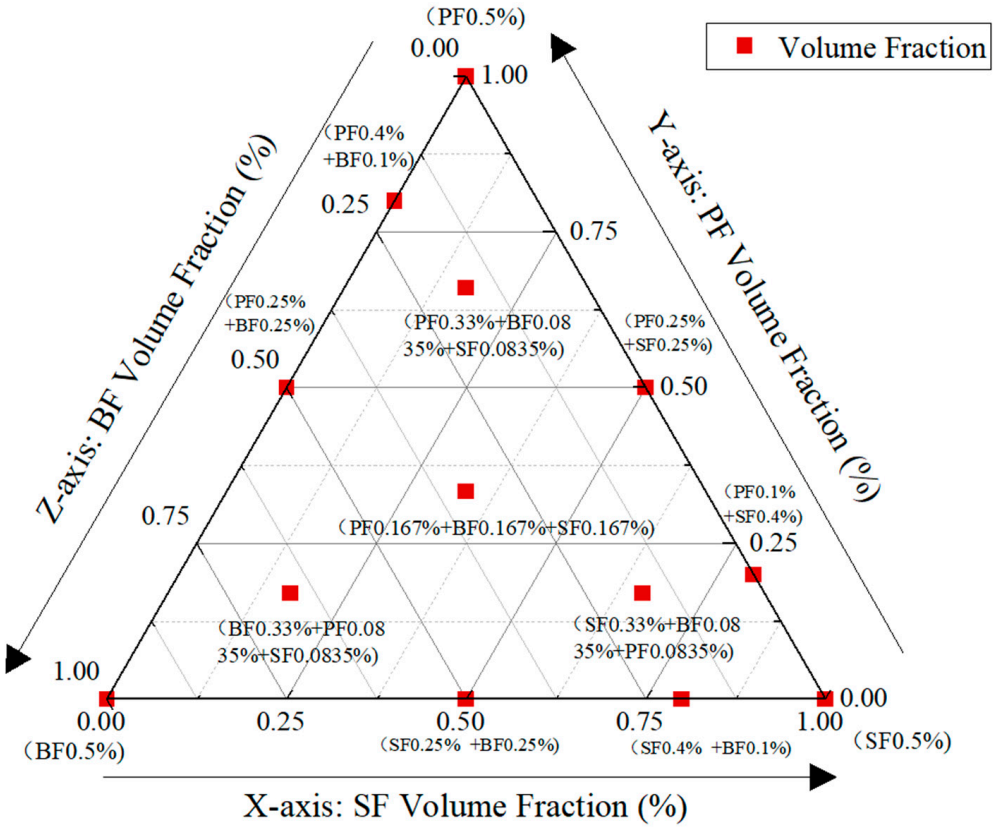


Figure 2. Simplex-centroid design diagram for fiber dosage.

In Figure 2, the coordinate axes represent the volume fractions of the components (x_{SF}, x_{PF}, x_{BF}). Any point within the diagram corresponds to the proportional combination of SF, PF, and BF, i.e., x_{SF}:x_{PF}:x_{BF}. The contour lines reflect the variation in concrete performance in response to changes in component volume fractions, and y_{pred} denotes the predicted performance value for a specific fiber proportion.

Table 4. Fiber dosage (kg/m^3).

Group ID	SF	BF	PF	Total Fiber
GPC	0	0	0	0
GPS0.5	39.25	0	0	39.25
GPP0.5	0	0	4.65	4.65
GPB0.5	0	13.30	0	13.30
GPS0.25B0.25	19.63	6.65	0	26.28
GPS0.4B0.1	31.40	2.66	0	34.06
GPS0.25P0.25	19.63	0	2.33	21.96
GPS0.4P0.1	31.40	0	0.93	32.33
GPP0.25B0.25	0	6.65	5.81	12.46
GPP0.4B0.1	0	2.66	3.72	6.38
GPS0.33BP	25.91	2.26	0.82	28.98
GPSB0.33P	6.67	0.79	8.78	16.24
GPSBP0.33	6.67	2.26	3.07	12.00
GPSBP0.167	13.11	4.44	1.55	19.10

Note: GPC represents plain geopolymer concrete. GPS0.5 indicates GPC with 0.5% SF by volume. GPS0.25B0.25 denotes a hybrid GPC containing 0.25% SF and 0.25% BF. GPS0.33BP corresponds to a ternary hybrid system with 0.33% SF, 0.0835% BF, and 0.0835% PF, maintaining the total fiber dosage constraint of 0.5%.

2.3. Test Methods

2.3.1. Compressive Strength Test

Compressive strength tests on fiber-reinforced geopolymer concrete (FRGPC) were primarily conducted according to Chinese standards [43,44]. Since non-standard cube specimens were used, the size effect correction factor for compressive strength was adopted as 0.95 according to CECS 13:2009. The compressive strength was calculated using Equation (2):

$$f_c = 0.95 \times \frac{F}{A_c} \quad (2)$$

where F represents the failure load of the specimen (N), and A_c is the bearing area of the specimen (mm^2).

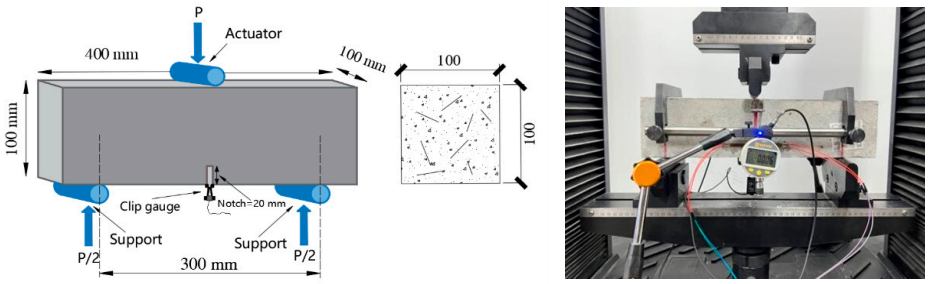
2.3.2. Three-Point Bending Test

Three-point bending tests were conducted on 100 mm × 100 mm × 400 mm notched beams with a span of 300 mm according to RILEM TC162-TDF [45]. A prefabricated mid-span notch (20 mm depth) was formed at the beam bottom. To form the notch, a 100 mm × 20 mm × 2 mm acrylic plate was fixed using welding adhesive in the mold 24 h before casting. The concrete was then poured, vibrated, covered with film, demolded after 24 h, and immersed in water for curing until testing.

The tests were performed under a displacement-controlled procedure using a universal testing machine (MTS E45) at a loading rate of 0.2 mm/min. The parameters of the testing machine are listed in Table 5. Schematic diagrams of the specimen configuration and test setup are presented in Figure 3.

Table 5. Parameters of MTS E45.

Specification Item	Technical Parameter
Maximum Rated Force (kN)	100
Minimum Test Speed (mm/min)	0.001
Position Resolution (mm)	0.000017
Maximum Specimen Length (mm)	600



(**a**) (**b**)

Figure 3. Schematic diagram of three-point bending test: (**a**) specimen schematic; (**b**) test setup.

2.3.3. Early-Age Shrinkage Test

The fresh mixture was poured into 100 mm × 100 mm × 400 mm prism molds. After molding, the specimens were transferred to a curing room for 24 h, at a temperature of 20 ± 2 °C and a humidity of about 95 ± 2%. Thereafter, the concrete prisms were demolded, marked, and transferred to a laboratory environment maintained at 20 ± 2 °C and 55 ± 15% relative humidity for the measurement of early-age GPC specimen shrinkage. A vertical length comparator was used as the test apparatus. The frame of this instrument was equipped with a dial gauge with a precision of 0.01 mm. This setup was employed to measure the shrinkage deformation of the GPC specimens over a period of 28 days, as illustrated in Figure 4. Prior to testing, the extensometer was calibrated and zeroed to ensure measurement accuracy.



(**a**) (**b**)

Figure 4. Shrinkage test setup: (**a**) vertical shrinkage testing apparatus; (**b**) dial gauge.

The shrinkage values of concrete were calculated using Equation (3):

$$\varepsilon_{st} = \frac{L_0 - L_t}{L_b} \tag{3}$$

where ε_{st} is shrinkage strain at testing age t (days), t is counted from the initial length measurement; L_b is the gauge length of the specimen, equivalent to the measurement span of the contact-type extensometer (mm); L_0 is the initial length reading of the specimen (mm); and L_t is the length reading of the specimen at testing age t (days) (mm).

2.3.4. SEM Microstructural Analysis

Specimen microstructural morphology was analyzed using a scanning electron microscope (SEM). To maintain the integrity of the post-failure microstructure, all samples were extracted from specimens that had fractured during splitting tensile tests. The specimens had dimensions ranging from 3 to 10 mm. A JSM-6490LV tungsten-filament SEM was used

for testing. The samples were secured onto aluminum stubs with conductive adhesive tape and placed in the chamber. Images were captured at various locations and magnification levels to characterize the fracture surfaces and interfacial transitions.

3. Results and Discussion

3.1. Analysis of Compressive Strength in FRGPC

The compressive strength test results for hybrid-fiber-reinforced GPC, designed via the simplex-centroid method, are summarized in Table 6; the corresponding contour map is shown in Figure 5.

Table 6. Cubic compressive strength of FRGPC.

Matrix ID	Compressive Strength (MPa)	Improvement Rate (%)	Matrix ID	Compressive Strength (MPa)	Improvement Rate (%)
GPC	54.2	0	GPS0.4P0.1	74.13	36.77
GPS0.5	67.55	24.63	GPP0.4B0.1	57.75	6.55
GPP0.5	63.80	17.71	GPP0.25B0.25	61.84	14.10
GPB0.5	59.46	9.70	GPS0.33BP	68.30	26.01
GPS0.25B0.25	69.34	27.93	GPSB0.33P	61.89	14.19
GPS0.4B0.1	70.13	29.39	GPSBP0.33	72.87	34.45
GPS0.25P0.25	71.48	31.88	GPSBP0.167	72.51	33.78

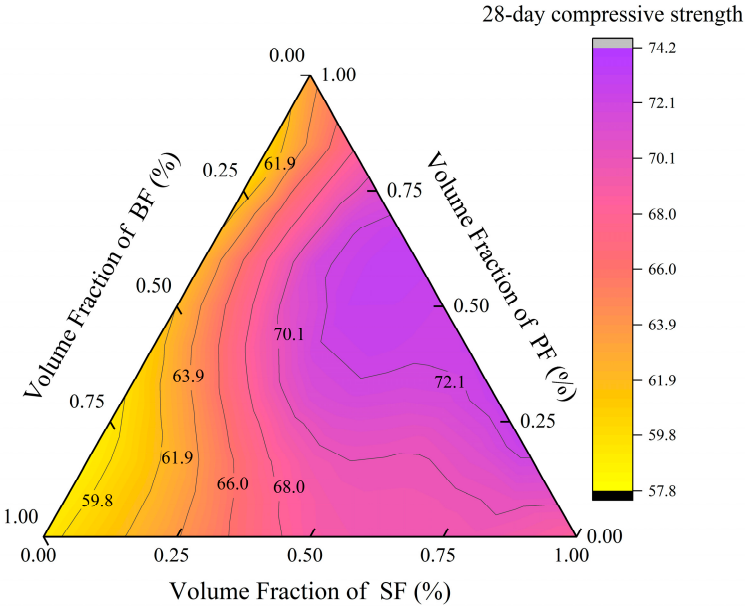


Figure 5. Contour plot of hybrid-fiber effects on 28-day compressive strength.

As shown in Table 6 and Figure 5, the incorporation of fibers positively influences the compressive strength of GPC. In single-fiber systems, SF incorporation exhibits the most significant improvement compared to fiber-free GPC, increasing compressive strength by 24.63%. Adding PF and BF leads to comparatively smaller enhancements, with compressive strength increases of 17.71% and 9.70%, respectively. The different efficiencies of fibers for enhancing the mechanical properties of GPC arise from the structural characteristics of the fibers themselves. SF and PF effectively bridge cracks within the concrete matrix, creating robust bridging effects that improve compressive strength. In addition, SF's high tensile strength and elastic modulus enable superior resistance to deformation and crack propagation under external loads.

In terms of hybrid-fiber systems, the SF–PF binary combination exhibits significant positive effects. The compressive strength initially increases and then decreases with rising PF content. When PF accounts for 5% to 75% of the total fiber volume, the compressive strength consistently exceeds 70 MPa, demonstrating an enhancement when SF and PF are used together. In the SF-BF binary system, the compressive strength increases monotonically with the SF content, reaching over 68 MPa when SF exceeds 50% of the total fiber content, indicating favorable positive hybrid effects. In contrast, the PF-BF binary combination shows minimal improvement and extensive negative hybrid effect zones, with the compressive strength lower than that of single-fiber systems at equivalent dosages. In ternary hybrid-fiber systems, higher proportions of SF (purple regions) are associated with the most significant enhancement in compressive strength; this is attributed to SF's dominant reinforcement effect. A high PF content (dark yellow regions) provides moderate improvement, though its contribution is less pronounced than SF's. Conversely, a high BF content (light yellow regions) induces extensive negative hybrid effects, resulting in degraded compressive strength.

The quantitative relationship between compressive strength and hybrid-fiber volume is expressed by Equation (4), with an R^2 of 0.839:

$$f_c = 13.73x_1 + 9.04x_2 + 4.70x_3 + 30.90x_1x_2 + 17.95x_1x_3 - 4.12x_2x_3 + 78.61x_1x_2x_3 \quad (4)$$

where x_1, x_2, and x_3 represent the volume fractions of SF, PF, and BF, respectively.

Equation (4) indicates that the coefficient β_1 (SF) exceeds both β_2 (PF) and β_3 (BF), thereby confirming that SF has a dominant contribution to the enhancement of compressive strength, which is consistent with the previous analysis. The positive values of coefficients β_{12} (SF-PF interaction) and β_{13} (SF-BF interaction), in contrast to the negative value of β_{23} (PF-BF interaction), suggest that the substitution of SF for PF or BF leads to an improvement in compressive strength, while combining PF and BF results in a reduction in strength. Furthermore, the positive value of β_{123} (ternary interaction) demonstrates an overall synergistic effect on compressive strength.

Steel fibers exhibit a higher elastic modulus and tensile strength, which leads to more pronounced reinforcement efficiency. Polypropylene fibers, characterized by their fine diameter and large specific surface area, enable a uniform distribution within the concrete matrix, effectively absorbing and dispersing stress during compression to prevent stress-induced failure. As structural fibers, SF and PF complement each other, producing a synergistic effect: SF primarily bridges cracks and resists tensile forces, while PF disperses stress and inhibits crack propagation. This dual reinforcement mechanism significantly enhances the overall performance of GPC. In contrast, the smaller diameter and tendency to form bundles of BF result in a substantially higher fiber count compared to SF and PF at equivalent volume fractions. When BF volumes exceed 50% of the total fiber content, inadequate dispersion leads to fiber clustering, which amplifies negative hybrid effects as the BF dosage increases.

3.2. Effect of Fibers on the Flexural Strength of GPC

Figure 6 illustrates the flexural strength of hybrid-fiber-reinforced geopolymer concrete (HFRGPC). The quantitative relationship between flexural strength, fb, and hybrid-fiber reinforcement is given by Equation (5), with an R^2 of 0.896:

$$f_b = 2.66x_1 + 2.97x_2 + 1.19x_3 + 2.20x_1x_2 + 0.77x_1x_3 - 3.32x_2x_3 - 28.33x_1x_2x_3 \quad (5)$$

where f_b is the flexural strength, and x_1, x_2, and x_3 represent the volume fractions of SF, PF, and BF, respectively.

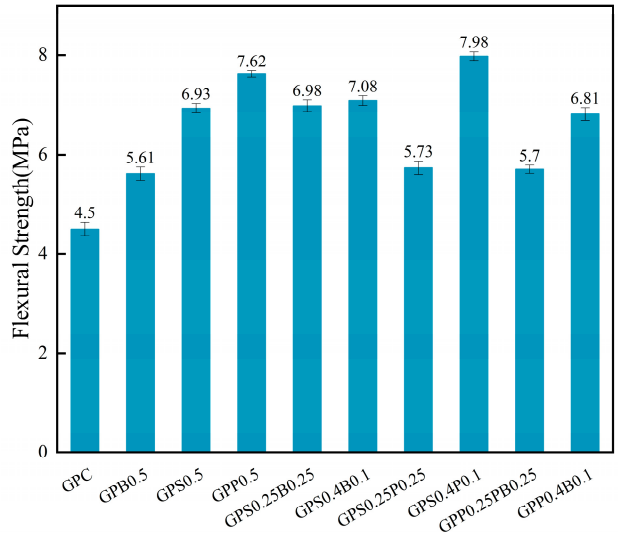


Figure 6. Flexural strength of HFRGPC.

As shown in Figure 6, both single- and hybrid-fiber systems significantly improve the flexural performance of geopolymer concrete. The fiber–matrix bridging mechanism plays a critical role in suppressing crack development under flexural stress, leading to enhanced strength and deformation capacity [46–48]. Polypropylene fiber (PF, mix GPP0.5) yields the most pronounced enhancement in flexural strength, exhibiting a 69.3% increase over the plain GPC. Steel fiber (SF, mix GPS0.5) demonstrates a moderate improvement of 54.0%, while basalt fiber (BF, mix GPB0.5) provides a more modest gain of 24.7%. Equation (5) confirms that the coefficient β_2 (PF) exceeds the coefficients β_1 (SF) and β_3 (BF), thereby demonstrating PF's dominant contribution to flexural strength, and the regression results are in close agreement with experimental data. Both SF and PF, classified as structural fibers, effectively transfer tensile stresses across cracks under bending loads, thereby restricting deformation and crack propagation. Although PF possesses a lower elastic modulus and tensile strength than SF, its higher fiber number per unit volume and larger specific surface area facilitate uniform dispersion, effectively controlling microcrack development. The randomly oriented three-dimensional distribution of PF absorbs and redistributes strain energy from both external and internal stresses. Notably, the incorporation of PF mitigates early-age microcracking, thereby improving early-stage performance [49].

Figure 7 presents a ternary contour map illustrating the influence of the different types of fibers on flexural strength. In SF-PF binary systems, when the content of PF is below 75% of the total fiber content, flexural strength initially increases and then decreases with increasing PF content. The SF-PF combination exhibits a moderately positive effect on flexural strength. In contrast, BF-containing binary systems (SF-BF and PF-BF) show minimal improvement, as flexural strength progressively decreases with increasing BF content. This observation aligns with Equation (5), where the positive values of β_{12} (the SF-PF interaction coefficient) and β_{13} (the SF-BF interaction coefficient) and the negative value of β_{23} (the PF-BF interaction coefficient) indicate that substituting SF for PF/BF improves flexural strength, while PF-BF combinations reduce it. In the ternary hybrid-fiber system, a high SF or PF content (indicated by the purple and pink regions) significantly enhances flexural strength. However, for other fiber ratios, extensive negative hybrid effect zones (yellow regions) impair flexural strength. The negative β_{123} (ternary interaction term) confirms an overall weakening effect on flexural strength. Notably, high BF content (black regions) induces severe degradation, resulting in the flexural strength falling below that of single-fiber BF systems at equivalent volume fractions.

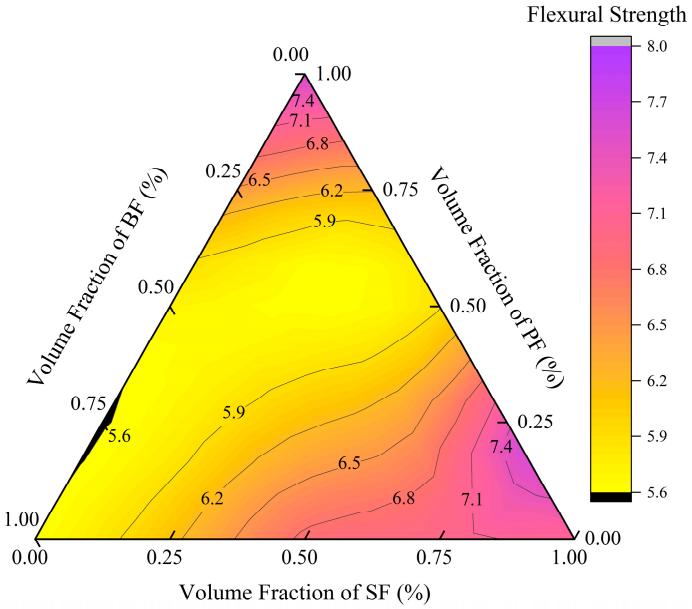


Figure 7. Contour of hybrid-fiber effects on flexural strength.

The decline in performance is attributed to the non-uniform dispersion of BF at high volume fractions, which leads to increased internal porosity and weakens the interfacial bond between aggregates and the geopolymer matrix. This, in turn, compromises the flexural strength [50].

3.3. Effect of Fibers on the Load–Deflection Curve of GPC

Figure 8 demonstrates the load–deflection curves of FRGPC beams. The flexural toughness indices of each FRGPC group were calculated and are summarized in Table 7.

Table 7. Flexural strength and toughness of FRGPC beams.

Matrix ID	f_L /MPa	f_u /MPa	$D_{f,2}$ /kN·mm	$D_{f,3}$ /kN·mm	$f_{eq,2}$ /MPa	$f_{eq,3}$ /MPa	$f_{R,2}$ /MPa	$f_{R,3}$ /MPa
GPC	4.50	4.50	—	—	—	—	—	—
GPS0.5	6.51	6.93	4.05	10.05	5.70	2.83	2.24	1.17
GPB0.5	5.61	5.61	1.19	2.80	1.67	0.79	0.81	—
GPP0.5	6.89	7.62	2.16	9.51	3.04	2.68	2.49	2.71
GPS0.25B0.25	6.89	6.98	1.72	4.16	2.42	1.17	1.03	0.42
GPS0.4B0.1	6.96	7.08	2.61	5.72	3.67	1.61	1.31	0.96
GPS0.25P0.25	5.71	5.73	3.84	15.18	5.40	4.27	4.50	3.67
GPS0.4P0.1	7.69	7.98	4.68	13.68	6.59	3.85	3.94	1.78
GPP0.25B0.25	5.28	5.70	1.11	4.49	1.57	1.26	1.38	1.28
GPP0.4B0.1	5.86	6.81	1.45	3.81	2.03	1.07	1.26	—
GPSPB0.33	5.01	5.77	0.34	0.84	0.48	0.24	0.46	—
GPS0.33PB	6.49	6.52	4.18	10.32	5.87	2.90	3.14	0.99
GPSP0.33B	5.67	5.67	0.86	1.92	1.21	0.54	0.95	—
GPSPB0.167	6.02	6.02	1.08	3.02	1.52	0.85	0.78	—

Note: f_L denotes the first-crack strength; f_u represents the ultimate flexural strength; $D_{f,2}$ and $D_{f,3}$ indicate the flexural toughness energy absorption values; $f_{eq,2}$ and $f_{eq,3}$ signify the equivalent flexural strengths; "$f_{R,2}$" and "$f_{R,3}$" correspond to the residual flexural strengths; and "—" indicates non-measurable values, primarily applicable to the plain control specimens (GPC).

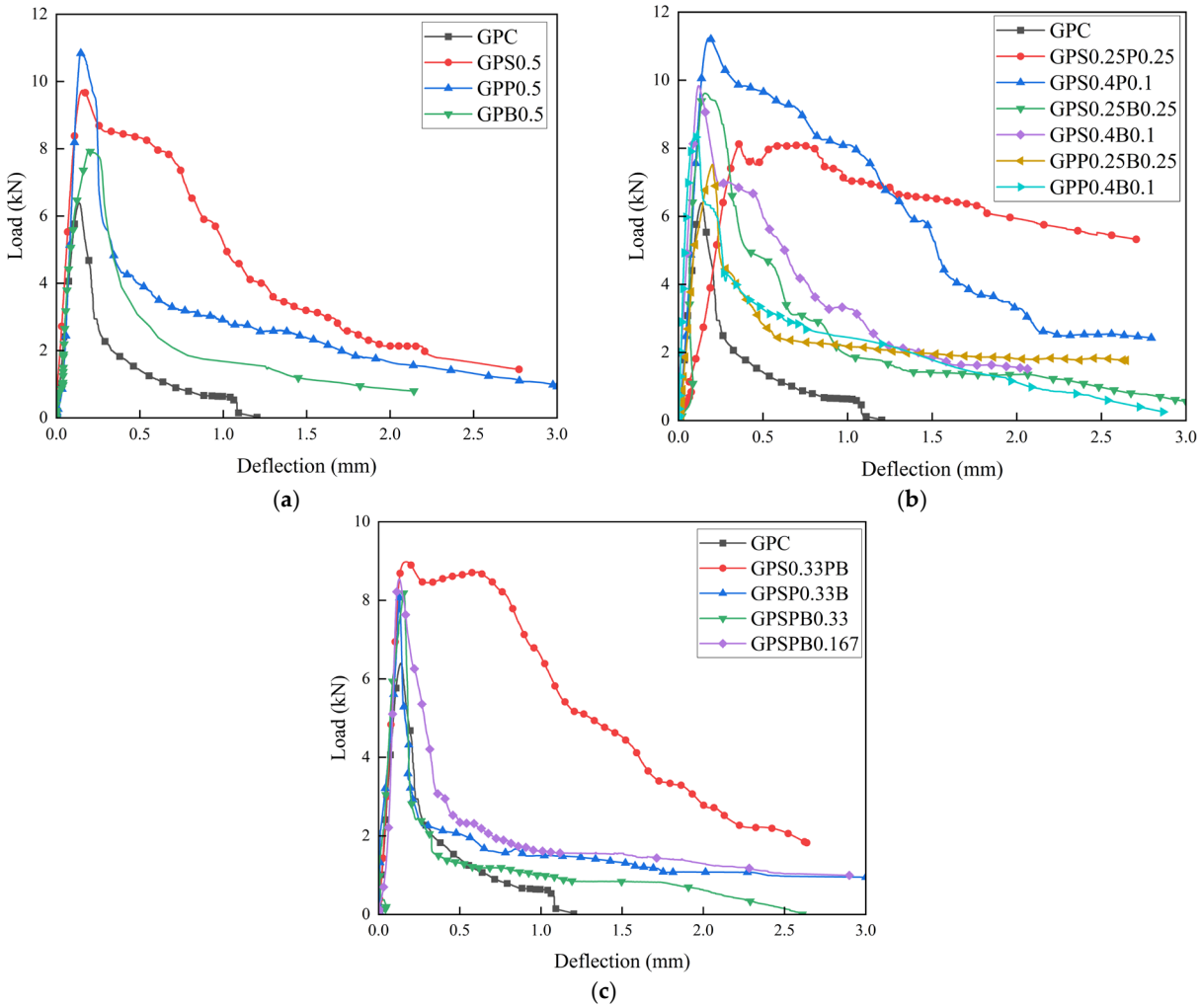


Figure 8. Load–deflection curves of FRGPC beams: (**a**) single-fiber system; (**b**) dual-fiber hybrid system; (**c**) ternary-fiber hybrid system.

As shown in Figure 8a, the toughness of GPC was significantly enhanced by the incorporation of various fibers. These fibers can sustain tensile stresses during crack propagation through crack bridging, restricting lateral deformation of the specimens and thereby markedly improving their deformation capacity. During concrete cracking, fibers function as "stress-transfer reinforcements," substantially enhancing flexural toughness. Table 7 indicates that in single-fiber systems, GPS0.5 achieved an $f_{eq,2}$ of 5.70 MPa and an $f_{R,2}$ of 2.24 MPa, both of which are significantly higher than the same values for GPB0.5. Notably, GPP0.5 demonstrates unique ductility characteristics; while its $f_{eq,2}$ (3.04 MPa) is lower, its residual strength (2.49 MPa) approaches that of SF systems, indicating the effectiveness of PF in constraining deformation during later cracking stages. These results confirm that both SF and PF significantly contribute to post-crack load-bearing capacity, with SF demonstrating a superior toughness enhancement compared to PF.

Figure 9 presents a ternary contour map that illustrates the effects of using hybrid-fiber systems on flexural toughness, denoted as $f_{eq,2}$ and $f_{R,2}$. The SF-PF hybrid system demonstrates optimal synergistic effects, with GPS0.4P0.1 exhibiting increases of 15.6% in $f_{eq,2}$ (6.59 MPa) and 75.9% in $f_{R,2}$ (3.94 MPa) compared to SF-only systems. When the volume fraction of PF remains below 42% of the total fiber content, the hybrid system maintains $f_{eq,2}$ values above 5.8 MPa, with $f_{R,2}$ values exceeding 3.0 MPa, suggesting the formation of a continuous high-toughness zone. Although $f_{eq,2}$ gradually decreases when the PF content surpasses 42%, it remains superior to single-fiber systems using PF at equivalent

dosages. This observation suggests that while excessive PF may weaken SF-PF synergy, SF continues to provide essential load-bearing support, thereby maintaining high system strength. These findings are consistent with previous studies [51,52] that confirm that hybrid systems combining SF (high-modulus) and PF (low-modulus) effectively enhance the deformation capacity of concrete.

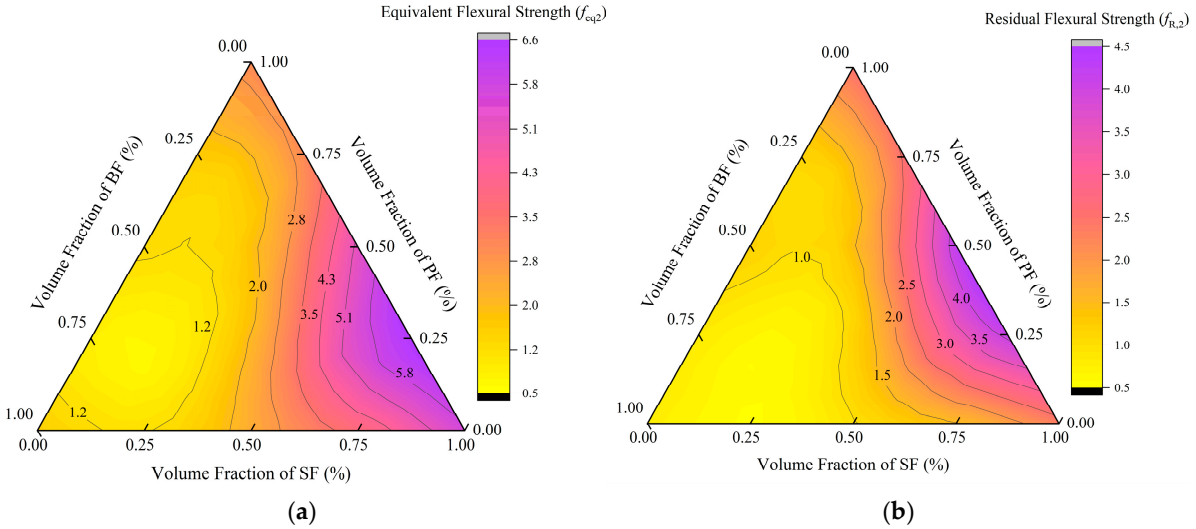


Figure 9. Contour of hybrid-fiber effects on flexural toughness: (**a**) $f_{eq,2}$; (**b**) $f_{R,2}$.

In contrast, BF hybrid systems demonstrate inferior performance. When compared to single-fiber SF systems, the flexural toughness index of specimen GPS0.25B0.25 decreased by 42.5% in terms of $f_{eq,2}$ and by 46.0% in terms of $f_{R,2}$, indicating significant negative effects. The chopped BFs utilized in the present study, which are classified as non-structural fibers with shorter lengths, have limited capacity to bridge macrocracks and restrict lateral deformation in concrete compared with structural fibers.

In the ternary hybrid-fiber system, the trends of fiber reinforcement on $f_{eq,2}$ and $f_{R,2}$ were found to be similar. SF demonstrated significant enhancement of the equivalent flexural strength at medium-to-high volume fractions (purple and pink regions). PF provided some improvement in equivalent flexural strength at larger volume fractions, although the magnitude of this enhancement was slightly lower than that achieved by steel fibers (dark yellow regions). Furthermore, at higher BF volume fractions, areas exhibiting a negative hybrid effect were observed (bright yellow regions). This phenomenon hinders any improvement in flexural strength.

The quantitative relationships for $f_{eq,2}$ and $f_{R,2}$ in the presence of hybrid-fiber reinforcement are given by Equation (6) (with an R^2 of 0.892) and Equation (7) (with an R^2 of 0.882):

$$f_{eq,2} = 6.12x_1 + 2.70x_2 + 1.56x_3 + 5.49x_1x_2 - 5.53x_1x_3 - 4.05x_2x_3 - 36.28x_1x_2x_3 \quad (6)$$

$$f_{R,2} = 2.41x_1 + 2.06x_2 + 0.91x_3 + 9.39x_1x_2 - 2.21x_1x_3 - 2.20x_2x_3 - 39.61x_1x_2x_3 \quad (7)$$

From Equation (6), it is evident that the value of coefficient β_1 (SF) significantly exceeds that of both β_2 (PF) and β_3 (BF), thereby confirming the dominant effect of SF on $f_{eq,2}$. The similarity of β_1 to β_2 from Equation (7) indicates that the enhancement efficiencies of the PF and SF systems in terms of $f_{R,2}$ are comparable. Both equations give a positive value for β_{12}, while yielding negative values for β_{13} and β_{23}, indicating that SF-PF hybridization effectively enhances deformation capacity. Conversely, BF-containing combinations show negative hybrid effects. The substantial negative values for β_{123} fur-

ther confirm the detrimental impact of ternary systems on flexural toughness, which is consistent with experimental observations and supports the high predictive accuracy of the regression models.

3.4. Effect of Fibers on Early-Age Shrinkage of GPC

Figure 10 illustrates the 28-day shrinkage values for single-fiber GPC. The early-age shrinkage value curve for GPC can be divided into three distinct phases: rapid growth, slow growth, and stabilization. During the initial 0–3 days, GPC experiences rapid shrinkage, with approximately 70% of the total shrinkage occurring within this period. This accelerated shrinkage is attributed to the highly active polymerization reaction in GPC during the first three days, which significantly reduces the free water content and leads to considerable volumetric contraction. From days 3 to 14, the shrinkage values gradually decrease, indicating a slow growth phase where cumulative shrinkage marginally increases with curing age. Beyond 14 days, the shrinkage values stabilize, and the total shrinkage remains nearly constant or exhibits a slight reduction as the curing age progresses.

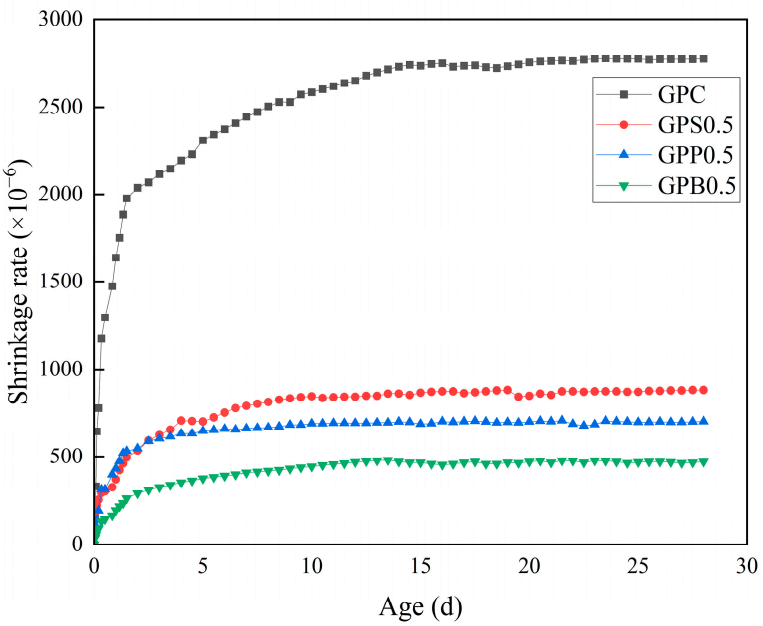


Figure 10. Plot of 28-day shrinkage values of single-fiber GPC.

As shown in Figure 10, the highest shrinkage of 2775 με was observed for GPC without fibers. The incorporation of fibers significantly reduced the early-age shrinkage of GPC. Among the three types of fibers tested, GPB0.5 demonstrated the most notable shrinkage inhibition effect, with a 28-day shrinkage value of 470 με, representing an 83.1% reduction compared to the reference GPC. The shrinkage values of GPS0.5 and GPP0.5 were 882.5 με and 705 με, corresponding to reductions of 68.2% and 74.6%, respectively [53].

The 28-day shrinkage value curves of dual-fiber GPC are presented in Figure 11. As shown, the incorporation of dual fibers produces significant synergistic effects in GPC. Hybrid systems that combine SF with other fiber types exhibit markedly enhanced shrinkage-restraining efficacy compared to systems using SF alone. Notably, the PF-BF hybrid system demonstrates exceptional performance: shrinkage is reduced by 80.1% relative to fiber-free GPC in GPB0.1P0.4, demonstrating a level of reduction comparable to that of GPB0.5. Furthermore, the GPB0.25P0.25 system achieves the highest shrinkage reduction, lowering the shrinkage value by 90.9%. This performance surpasses that of GPB0.5 and confirms the strong positive hybrid effects of dual-fiber systems. The shrinkage-inhibiting mechanism associated with SF and PF is primarily attributed to the rigid skeleton functions of the fibers.

During the early hydration stage, the fibers enhance the interfacial bond strength within the concrete matrix, providing a physical restraint against shrinkage deformation and resisting the internal capillary pressure of the matrix, thereby effectively reducing shrinkage values [54,55]. The large specific surface area and high water absorption capacity of BF enable it to interact with the matrix both physically and chemically. The fiber molecules attract free water, facilitating the formation of additional hydration products on the fiber surface. The combined action of physical and chemical forces enhances the interfacial bond strength, which restrains the shrinkage deformation induced by tensile stress in the fibers. This dual-force mechanism improves the overall bonding performance at the interface [56,57]. Furthermore, the hybrid system using PF and BF achieves an ultra-high shrinkage inhibition rate (90.9%), primarily due to the synergistic effect of a "rigid–flexible composite constraint". For this, the rigid skeleton of PF provides macroscopic restraint, while the flexible BF regulates the water film within the interfacial zone, mitigating internal humidity gradient changes and resulting in a more uniform stress distribution [47].

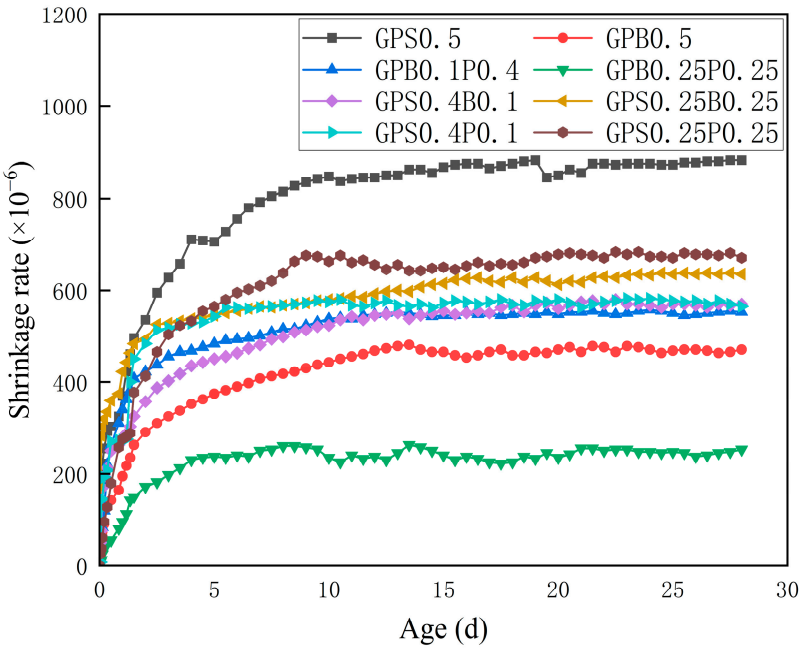


Figure 11. Plot showing 28-day shrinkage values of dual-fiber GPC.

GPC exhibits significant intrinsic shrinkage that can be effectively mitigated through fiber incorporation. Figure 12 presents a contour map illustrating the effects of hybrid-fiber systems on the 28-day shrinkage values of GPC. The PF-BF hybrid system demonstrates notable efficacy in restraining shrinkage: as the dosage of BF increases, the shrinkage value initially decreases and then begins to rise. When the proportion of BF exceeds 60% of the total fiber content, the shrinkage value increases with further BF addition, although it remains at a relatively low level, indicating a synergistic effect in shrinkage reduction between BF and PF.

In contrast, the SF-PF hybrid system exhibits limited shrinkage reduction, with negative hybrid effects predominating across multiple regions, leading to higher shrinkage values compared to single-fiber systems at equal dosages. For ternary hybrid systems, high proportions of BF result in significant reductions in shrinkage (green zones), while moderate dosages provide only minor improvements (light yellow zones). Conversely, high dosages of SF or PF introduce extensive negative hybrid effects (dark yellow zones) that counteract shrinkage mitigation.

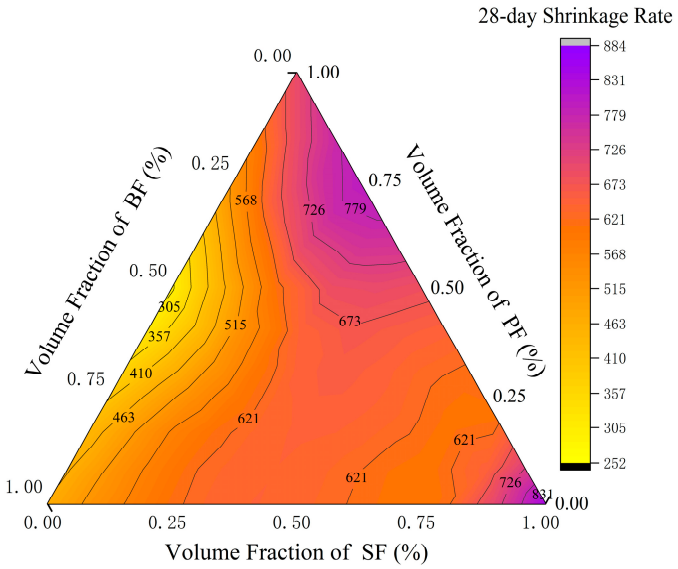


Figure 12. Contour of hybrid-fiber effects on the 28-day shrinkage values of GPC.

The quantitative relationship between early-age shrinkage values and hybrid-fiber reinforcement in GPC is given by Equation (8), with an R^2 of 0.714:

$$\varepsilon = 2.41x_1 + 2.06x_2 + 0.91x_3 + 9.39x_1x_2 - 2.21x_1x_3 - 2.20x_2x_3 - 39.61x_1x_2x_3 \quad (8)$$

Equation (8) shows that the coefficient β_3 (BF) exceeds both β_1 (SF) and β_2 (PF), thereby confirming the superior efficacy of BF in suppressing shrinkage in single-fiber systems. Furthermore, all binary interaction coefficients (β_{12}, β_{13}, β_{23}) are positive, indicating significant positive hybrid effects in dual-fiber systems. In contrast, the large negative β_{123} (ternary interaction) signifies significant detrimental hybrid effects in three-fiber combinations.

3.5. Fiber Microscopic Reinforcement Mechanism

As previously stated, different hybrid-fiber systems exhibit significant variations in terms of their effects on the compressive strength, flexural performance, and shrinkage suppression of GPC. The underlying cause of these performance differences lies in the interactions between the fiber's scale characteristics and the matrix, which can be verified through microstructural observations. Figure 13 presents scanning electron microscopy (SEM) images of various fiber types within GPC. As illustrated in Figure 13a,b, SFs are firmly embedded in the matrix, demonstrating strong interfacial bonding, with hydration products adhering to their surfaces. Due to their longer length and larger diameter, SFs effectively bridge macrocracks. The primary modes of energy dissipation and failure for SF are debonding and pull-out, with fracture occurring relatively rarely. This indicates that the large diameter and small surface area of SF prevent fracture; even when interfacial shear stress leads to debonding, the internal tensile stress remains below critical levels. Consequently, SF provides sustained and effective reinforcement and toughening to the concrete.

Polypropylene fibers (PFs) primarily fail through debonding and fracture, with fractured fibers exhibiting high elongation, which enhances the toughness of concrete. Figure 13c illustrates the residual strain traces at fracture sites, revealing elongated deformation patterns that corroborate PF's role in improving toughness. In contrast, basalt fibers (BFs), despite their smaller monofilament length and diameter, effectively bridge microcracks within the GPC matrix, dispersing stress and inhibiting crack propagation. When a BF intersects a propagating crack, the crack deflects along the fiber's path, extending into the GPC matrix. This crack deflection, as well as the formation of new interfaces, dissipates

substantial energy. Under tensile stress, the primary reinforcement mechanisms of BF are fiber pull-out and fracture, which collectively enhance crack resistance and toughness.

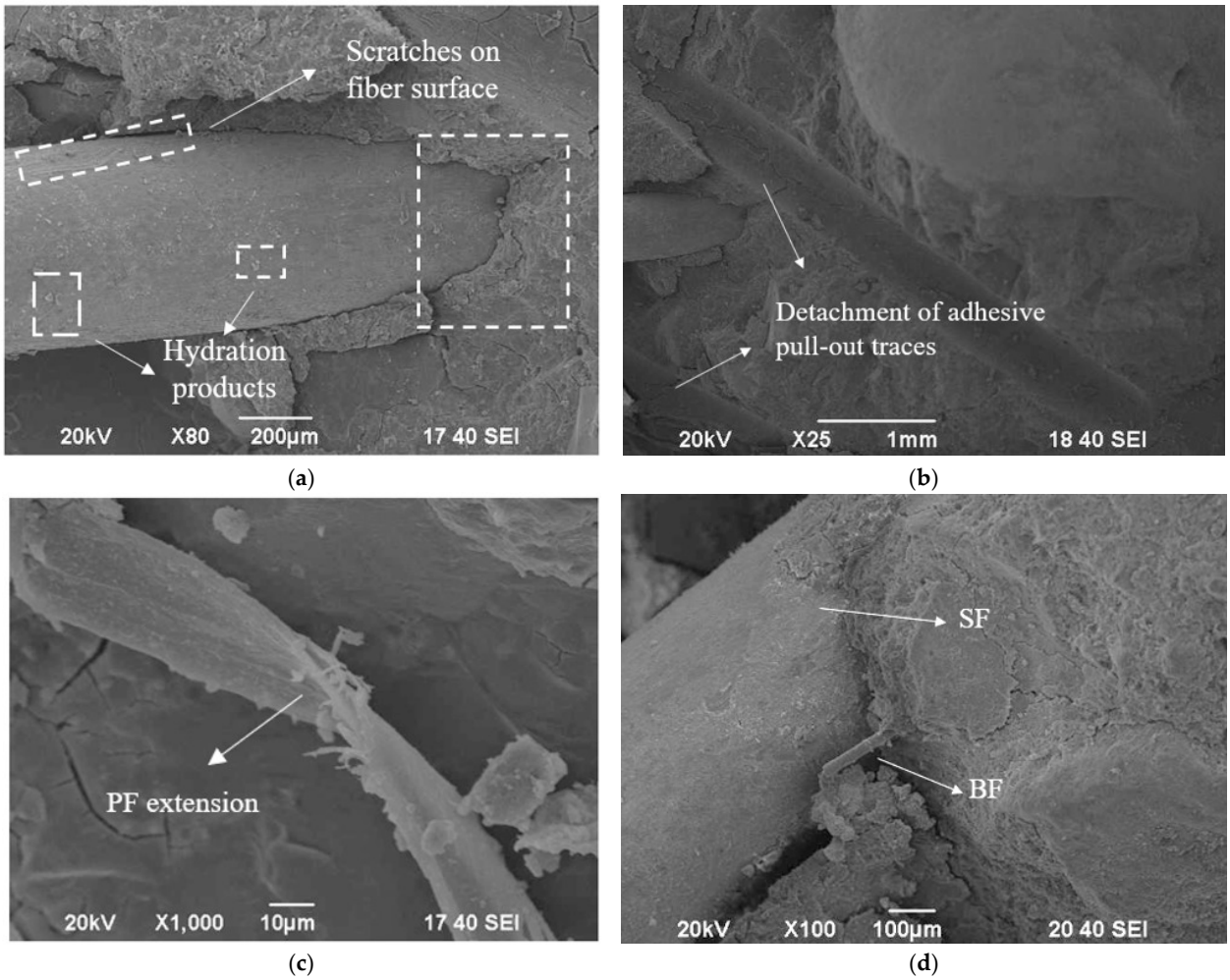


Figure 13. Microstructure of GPC with different fiber contents: (**a**) SF; (**b**) SF pull-out traces; (**c**) PF; (**d**) BF.

In HFRGPC systems, fibers with varying properties can contribute to crack-resisting effects at different stages of crack development, leading to diverse energy dissipation and failure modes. As illustrated in Figure 14, the primary reinforcement mechanisms include fiber bridging, fiber pull-out, and crack deflection. When GPC is subjected to external loads and experiences damage, microcracks initially form within the matrix, gradually propagating into macrocracks that ultimately lead to specimen failure. During the initial loading stage of concrete (microcrack phase), polypropylene fibers, owing to their excellent dispersibility, effectively bridge these microcracks, inhibiting their propagation into macrocracks. This role is particularly critical during the plastic and early elastic stages of concrete [58,59]. When microcracks develop into macrocracks, steel fibers, with their high elastic modulus and tensile strength, begin to play a dominant role. The longer SFs can span macrocracks, connect the matrix on both sides of the crack through strong bridging effects, and continue to transfer stress. This enables the concrete to retain load-bearing capacity even after visible cracking, manifesting as a slow decline in the post-peak segment of the load–deflection curve, i.e., a significant improvement in toughness [60]. The continuation of the bridging effect is ultimately reflected in the fiber pull-out process. The pull-out behavior and energy dissipation mechanisms of SF and PF are fundamentally different, forming a complementary mechanism [61]. In contrast, BF, which has a smaller diameter and a denser

distribution, effectively bridges microcracks within the matrix. Through mechanisms such as crack deflection and fiber pull-out, BF significantly constrains microcrack propagation, thereby enhancing the mechanical strength and crack resistance of GPC. This hierarchical synergy is critical for optimizing the performance of HFRGPC systems.

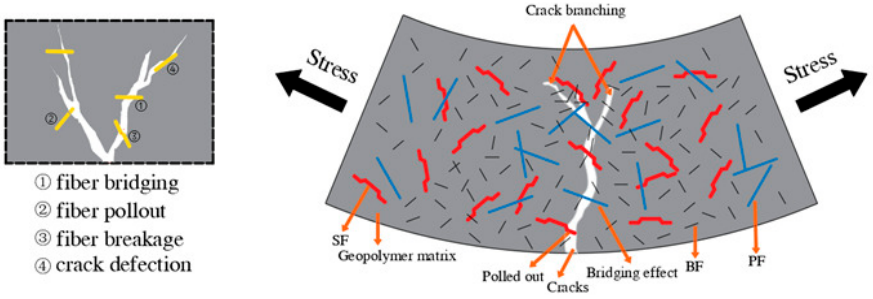


Figure 14. Schematic diagram of the enhancement mechanism of multiscale fibers on GPC.

3.6. Determination of the Optimal Mix Proportion

Previous studies indicate that overlaying simplex-centroid mixture experiment contours can address specific performance requirements for concrete [62,63]. Based on the findings of this study, the optimal hybrid proportions of fibers for GPC were identified to satisfy comprehensive performance criteria, including compressive strength, flexural toughness, and shrinkage mitigation. The critical compressive strength threshold for GPC was set at $\geq$70 MPa. In addition, because the brittleness of the geopolymer matrix is higher at the same compressive strength level, resulting in the toughness of GPC being lower than that of OPCC, based on the classification of the highest level of residual flexural strength of concrete in the Chinese standard [64], the critical residual bending strength of HFRGPC was defined as being greater than 3.0 MPa. Simultaneously, based on the 28-day shrinkage values of fiber-reinforced geopolymer concrete reported in Li et al.'s experimental results, the critical shrinkage value for HFRGPC was defined as less than 650 $\times$ 10^{-6}. As a result, the contour lines corresponding to critical performance criteria (70 MPa compressive strength, 6 MPa flexural strength, 3.0 MPa residual strength, and 650 με shrinkage) [65,66] were extracted from Figures 5, 7, 9 and 12, respectively, and overlaid on a ternary diagram.

In Figure 15, the fiber combinations within the pink region meet all performance criteria. In this area, the SF volume fraction is equal to or greater than 55%, the PF volume fraction ranges from 13% to 46%, and the BF volume fraction is between 25% and 68% of the total fiber volume. This finding illustrates that hybridizing three distinct fibers in specific proportions produces positive synergies for compressive strength, flexural strength, toughness, and shrinkage performance in GPC, consistent with previous results of this study.

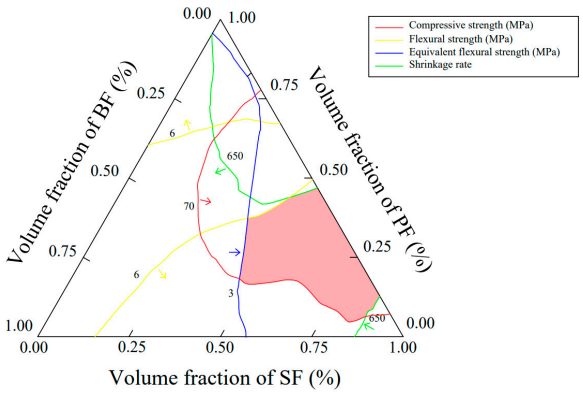


Figure 15. Optimal hybrid fiber volume dosage for GPC.

This study confirms the potential of the simplex-centroid method as an effective approach for optimizing hybrid fibers in GPC, thereby aiding in the design of fiber-reinforced composites or concrete. Additionally, by establishing the fibers used here as a benchmark, future research can utilize this method to achieve more precise optimization within narrower composition ranges.

4. Conclusions

This study utilized a simplex-centroid design to investigate the effects of SF, PF, and BF, both individually and in hybrid combinations, on the compressive strength, flexural strength, flexural toughness, and early-age shrinkage of fly ash–slag-based GPC. Quantitative predictive models and regression equations linking fiber combinations to performance responses were established to systematically elucidate the mechanisms behind reinforcement, toughening, and shrinkage reduction. The main conclusions drawn are as follows:

1. The hybrid-fiber system demonstrated a significant positive synergistic effect. The binary SF-PF combination yielded the most comprehensive improvement, with the optimal specimen (GPS0.4P0.1) achieving a 36.8% increase in compressive strength and a 77.3% increase in flexural strength; this composite also exhibited superior flexural toughness.
2. All the fibers studied effectively inhibited early-age shrinkage in geopolymer concrete. Among them, the PF-BF binary system demonstrated the best inhibition effect through a synergistic "rigid–flexible composite restraint" mechanism, reducing the shrinkage rate by 90.9%. The optimized ternary hybrid formulation successfully achieved a balance between good mechanical performance and significant shrinkage suppression.
3. Quantitative regression models reveal the interactions among SF, PF, and BF, as well as their influence on material properties. The combination of SF and PF shows a positive synergistic effect, improving mechanical strength and toughness, whereas combining PF and BF results in a negative synergistic effect.
4. Microscopic analysis revealed that the synergy stems from complementary, stage-specific mechanisms—BF bridges microcracks, PF enhances toughness through plastic deformation after fracture, and SF resists macrocrack propagation through pull-out—collectively improving the overall durability and toughness of GPC.
5. Contour overlay analysis identified the optimal formulation range, i.e., satisfying all target properties, for the ternary fiber composite. The recommended fiber volume fractions are steel fiber $\geq$55%, polypropylene fiber 13–46%, and basalt fiber 25–68%. Within this range, the fibers work synergistically, leading to a composite characterized by high strength, high toughness, and low shrinkage.

However, this study has several limitations. The research is restricted to SFs, PFs, and BFs of specific dimensions, which may limit the broader applicability of the findings. Additionally, the investigation primarily focuses on macroscopic mechanical properties and early-age shrinkage, lacking sufficient correlation and quantitative analysis of long-term durability and microscopic mechanisms such as fiber clustering. Furthermore, the established regression model is only applicable to the specific dosages and material systems utilized in this study, necessitating further validation of its predictive accuracy and generalizability in other conditions.

Based on these limitations, the following directions are suggested for future research: First, expand the range of fiber types and scales, such as glass fibers, plant fibers, and carbon nanofibers, to explore the possible engineering applications of different types of fiber. Second, employ advanced techniques, including X-ray computed tomography (X-CT), for three-dimensional visualization and precise characterization of fiber dispersion. Finally, clarify the underlying micromechanisms and evolution patterns of material performance

by studying long-term durability and multi-field coupling effects, such as sulfate attack, chloride penetration, and fatigue.

Author Contributions: Conceptualization, Z.L. and X.N.; methodology, Z.L. and X.N.; software, Z.L., J.L. and J.J.; validation, Z.L., L.L. and J.J.; formal analysis, Z.L. and J.J.; funding acquisition, J.L.; investigation, Z.L. and T.I.w.N.; resources, X.N., L.L., Y.L. and J.L.; data curation, Z.L. and R.S.; writing—original draft preparation, Z.L.; writing—review and editing, X.N., Y.L., R.S. and T.I.w.N.; supervision, X.N. and Y.L.; project administration, X.N. and Y.L. All authors have read and agreed to the published version of the manuscript.

Funding: The authors gratefully acknowledge the National Natural Science Foundation of China (grant number 51608100), Natural Science Fund project of Jilin Province Science and Technology Department (grant number 20230101331JC), and Science and Technology Project of Jilin Province Education Department (grant number JJKH20250883KJ).

Data Availability Statement: The data presented in this study are available on reasonable request from the corresponding author.

Conflicts of Interest: The authors declare no conflicts of interest.

References

1. Benhelal, E.; Zahedi, G.; Shamsaei, E.; Bahadori, A. Global strategies and potentials to curb CO_2 emissions in cement industry. *J. Clean. Prod.* **2013**, *51*, 142–161. [CrossRef]
2. Griffiths, S.; Sovacool, B.K.; Del Rio, D.D.F.; Foley, A.M.; Bazilian, M.D.; Kim, J.; Uratani, J.M. Decarbonizing the cement and concrete industry: A systematic review of socio-technical systems, technological innovations, and policy options. *Renew. Sustain. Energy Rev.* **2023**, *180*, 113291. [CrossRef]
3. Xu, J.; Guan, Y.; Oldfield, J.; Guan, D.; Shan, Y. China carbon emission accounts 2020–2021. *Appl. Energy* **2024**, *360*, 122837. [CrossRef]
4. Han, X.; Zhang, P.; Zheng, Y.; Wang, J. Utilization of municipal solid waste incineration fly ash with coal fly ash/metakaolin for geopolymer composites preparation. *Constr. Build. Mater.* **2023**, *403*, 133060. [CrossRef]
5. Provis, J.L. Alkali-activated materials. *Cem. Concr. Res.* **2018**, *114*, 40–48. [CrossRef]
6. Turner, L.K.; Collins, F.G. Carbon dioxide equivalent (CO_2-e) emissions: A comparison between geopolymer and OPC cement concrete. *Constr. Build. Mater.* **2013**, *43*, 125–130. [CrossRef]
7. Das, S.; Saha, P.; Jena, S.P.; Panda, P. Geopolymer concrete: Sustainable green concrete for reduced greenhouse gas emission–A review. *Mater. Today Proc.* **2022**, *60*, 62–71. [CrossRef]
8. Van Deventer, J.S.J.; Provis, J.L.; Duxson, P. Technical and commercial progress in the adoption of geopolymer cement. *Miner. Eng.* **2012**, *29*, 89–104. [CrossRef]
9. Zhou, X.; Shen, J. Micromorphology and microstructure of coal fly ash and furnace bottom slag based light-weight geopolymer. *Constr. Build. Mater.* **2020**, *242*, 118168. [CrossRef]
10. Su, L.; Fu, G.; Liang, B.; Sun, Q.; Zhang, X. Mechanical properties and microstructure evaluation of fly ash-Slag geopolymer foaming materials. *Ceram. Int.* **2022**, *48*, 18224–18237. [CrossRef]
11. Oderji, S.Y.; Chen, B.; Ahmad, M.R.; Shah, S.F.A. Fresh and hardened properties of one-part fly ash-based geopolymer binders cured at room temperature: Effect of slag and alkali activators. *J. Clean. Prod.* **2019**, *225*, 1–10. [CrossRef]
12. Thunuguntla, C.S.; Rao, T.G. Effect of mix design parameters on mechanical and durability properties of alkali activated slag concrete. *Constr. Build. Mater.* **2018**, *193*, 173–188. [CrossRef]
13. Abdellatief, M.; Abd Elrahman, M.; Abadel, A.A.; Wasim, M.; Tahwia, A. Ultra-high performance concrete versus ultra-high performance geopolymer concrete: Mechanical performance, microstructure, and ecological assessment. *J. Build. Eng.* **2023**, *79*, 107835. [CrossRef]
14. Zhang, S.; Li, Z.; Ghiassi, B.; Yin, S.; Ye, G. Fracture properties and microstructure formation of hardened alkali-activated slag/fly ash pastes. *Cem. Concr. Res.* **2021**, *144*, 106447. [CrossRef]
15. Maganty, S.T.; Subramaniam, K.V. Efficiency of Steel Fibers in Geopolymer and Portland Cement Concrete: Comparative Evaluation of Fiber Bonding and Crack Bridging Stress. *Cem. Concr. Compos.* **2025**, *159*, 105988. [CrossRef]
16. Xing, X.; Wang, B.; Luo, S.; Lin, F.; Wei, J.; Xu, W.; Hu, J.; Yu, Q. Preparation and formation mechanism of high-toughness organic polymers modified geopolymers. *Cem. Concr. Compos.* **2024**, *150*, 105578. [CrossRef]
17. Khan, S.U.; Ayub, T. PET fiber–reinforced engineered geopolymer and cementitious composites. *J. Mater. Civ. Eng.* **2022**, *34*, 06021010. [CrossRef]

18. Wallah, S.; Rangan, B.V. *Low-Calcium Fly Ash-Based Geopolymer Concrete: Long-Term Properties*; Curtin University of Technology: Bentley, Australia, 2006; p. 108.
19. Collins, F.; Sanjayan, J.G. Effect of pore size distribution on drying shrinking of alkali-activated slag concrete. *Cem. Concr. Res.* **2000**, *30*, 1401–1406. [CrossRef]
20. Li, Z.; Liu, J.; Ye, G. Drying Shrinkage of Alkali-Activated Slag and Fly Ash Concrete; A Comparative Study with Ordinary Portland Cement Concrete. Available online: https://repository.tudelft.nl/record/uuid:a3dd27c0-6815-4307-b6f6-527e4eeea83d (accessed on 1 February 2019).
21. Bernal, S.A.; Provis, J.L.; Brice, D.G.; Kilcullen, A.; Duxson, P.; Van Deventer, J.S. Accelerated carbonation testing of alkali-activated binders significantly underestimates service life: The role of pore solution chemistry. *Cem. Concr. Res.* **2012**, *42*, 1317–1326. [CrossRef]
22. Duan, P.; Yan, C.; Luo, W.; Zhou, W. Effects of adding nano-TiO_2 on compressive strength, drying shrinkage, carbonation and microstructure of fluidized bed fly ash based geopolymer paste. *Constr. Build. Mater.* **2016**, *106*, 115–125. [CrossRef]
23. Zhang, W.; Xue, M.; Lin, H.; Duan, X.; Jin, Y.; Su, F. Effect of polyether shrinkage reducing admixture on the drying shrinkage properties of alkali-activated slag. *Cem. Concr. Compos.* **2023**, *136*, 104865. [CrossRef]
24. Zhang, L.V.; Suleiman, A.R.; Allaf, M.M.; Marani, A.; Tuyan, M.; Nehdi, M.L. Crack self-healing in alkali-activated slag composites incorporating immobilized bacteria. *Constr. Build. Mater.* **2022**, *326*, 126842. [CrossRef]
25. Hosseinzadehfard, E.; Mobaraki, B. Corrosion performance and strain behavior of reinforced concrete: Effect of natural pozzolan as partial substitute for microsilica in concrete mixtures. *Structures* **2025**, *79*, 109397. [CrossRef]
26. Kasaniya, M.; Thomas, M.D.A.; Moffatt, E.G. Pozzolanic reactivity of natural pozzolans, ground glasses and coal bottom ashes and implication of their incorporation on the chloride permeability of concrete. *Cem. Concr. Res.* **2021**, *139*, 106259. [CrossRef]
27. Ganesh, A.C.; Muthukannan, M. Development of high performance sustainable optimized fiber reinforced geopolymer concrete and prediction of compressive strength. *J. Clean. Prod.* **2021**, *282*, 124543. [CrossRef]
28. Abdalla, J.A.; Hawileh, R.A.; Bahurudeen, A.; Jyothsna, G.; Sofi, A.; Shanmugam, V.; Thomas, B. A comprehensive review on the use of natural fibers in cement/geopolymer concrete: A step towards sustainability. *Case Stud. Constr. Mater.* **2023**, *19*, e02244. [CrossRef]
29. Ansari, M.A.; Shariq, M.; Mahdi, F. Influence of fibres characteristics on the engineering properties of geopolymer concrete-a review. *Mater. Today Proc.* **2023**, *93*, 12–19. [CrossRef]
30. Ma, J.; Yuan, H.; Zhang, J.; Zhang, P. Enhancing concrete performance: A comprehensive review of hybrid fiber reinforced concrete. *Structures* **2024**, *64*, 106560. [CrossRef]
31. Zhang, H.; Sarker, P.K.; Wang, Q.; He, B.; Jiang, Z. Comparative fracture properties of ambient-cured geopolymer concrete containing four different fibers in mono and hybrid combinations using digital image correlation. *J. Build. Eng.* **2024**, *89*, 109288. [CrossRef]
32. Behfarnia, K.; Behravan, A. Application of high performance polypropylene fibers in concrete lining of water tunnels. *Mater. Des.* **2014**, *55*, 274–279. [CrossRef]
33. Akhmetov, D.; Akhazhanov, S.; Jetpisbayeva, A.; Pukharenko, Y.; Root, Y.; Utepov, Y.; Akhmetov, A. Effect of low-modulus polypropylene fiber on physical and mechanical properties of self-compacting concrete. *Case Stud. Constr. Mater.* **2022**, *16*, e00814. [CrossRef]
34. Zhang, T.; Wang, K.; Lin, B.; Yao, Y. The enhancement mechanism of modified basalt fiber on the performance of geopolymer concrete. *Constr. Build. Mater.* **2024**, *417*, 135123. [CrossRef]
35. Xu, J.; Kang, A.; Wu, Z.; Xiao, P.; Gong, Y. Effect of high-calcium basalt fiber on the workability, mechanical properties and microstructure of slag-fly ash geopolymer grouting material. *Constr. Build. Mater.* **2021**, *302*, 124089. [CrossRef]
36. Li, L.; Shu, W.; Xu, H.; Rui, X.; Wang, Z.; Zeng, Y.; Jia, S.; Chen, T.; Zhu, Z. Experimental study on flexural toughness of fiber reinforced concrete beams: Effects of cellulose, polyvinyl alcohol and polyolefin fibers. *J. Build. Eng.* **2024**, *81*, 108144. [CrossRef]
37. Sukontasukkul, P.; Pongsopha, P.; Chindaprasirt, P.; Songpiriyakij, S. Flexural performance and toughness of hybrid steel and polypropylene fibre reinforced geopolymer. *Constr. Build. Mater.* **2018**, *161*, 37–44. [CrossRef]
38. Smarzewski, P.; Barnat-Hunek, D. Property assessment of hybrid fiber-reinforced ultra-high-performance concrete. *Int. J. Civ. Eng.* **2018**, *16*, 593–606. [CrossRef]
39. Li, N.; Shi, C.; Zhang, Z.; Zhu, D.; Hwang, H.-J.; Zhu, Y.; Sun, T. A mixture proportioning method for the development of performance-based alkali-activated slag-based concrete. *Cem. Concr. Compos.* **2018**, *93*, 163–174. [CrossRef]
40. Scheffe, H. The simplex-centroid design for experiments with mixtures. *J. R. Stat. Soc. Ser. B (Methodol.)* **1963**, *25*, 235–251. [CrossRef]
41. Chen, Y.; Liu, P.; Sha, F.; He, S.; Lu, G.; Yu, Z.; Chen, H. Preparation and performance of the ultra-high performance mortar based on simplex-centroid design method. *J. Mater. Res. Technol.* **2021**, *15*, 3060–3077. [CrossRef]
42. Jiao, D.; Shi, C.; Yuan, Q.; An, X.; Liu, Y. Mixture design of concrete using simplex centroid design method. *Cem. Concr. Compos.* **2018**, *89*, 76–88. [CrossRef]

43. *GB/T50081-2019*; Standard for Test Methods of Concrete Physical and Mechanical Properties. China Architecture & Building Press: Beijing, China, 2019. (In Chinese)
44. *CECS:13-2009*; Standard test methods for fiber reinforced concrete. China Planning Press: Beijing, China, 2010. (In Chinese)
45. Vandewalle, L.; Nemegeer, D.; Balázs, G.L.; Barr, B. RILEM TC 162-TDF: Test and design methods for steel fibre reinforced concrete: Bending test. *Mater. Struct.* **2000**, *33*, 3–5.
46. Yassin, A.M.; Mohie Eldin, M.; Hafez, M.A.; Elnaggar, M.A. The Flexural Behavior and Mechanical Properties of Super High-Performance Concrete (SHPC) Reinforced Using the Hybridization of Micro Polypropylene and Macro Steel Fibers. *Buildings* **2024**, *14*, 1887. [CrossRef]
47. Xu, J.; Pi, Z.; Huang, S.; Liu, Y.; Chen, Z.; Shen, Y. Hybrid Effect of Basalt and Polyacrylonitrile Fibers on Physico-Mechanical Properties of Tailing Mortar. *Buildings* **2024**, *14*, 639. [CrossRef]
48. Ma, L.; Zhen, C.; Zeng, Q.; Li, B. Experimental Investigation on the Mechanical Properties of Geopolymer Recycled Aggregate Concrete Reinforced with Steel-Polypropylene Hybrid Fiber. *Buildings* **2025**, *15*, 1723. [CrossRef]
49. Liang, N.; Hu, G.; Zhou, K.; Liu, X.; Zhou, X. Study on early-age cracking resistance of multi-scale polypropylene fiber reinforced concrete in restrained ring tests. *J. Sustain. Cem.-Based Mater.* **2024**, *13*, 1050–1062. [CrossRef]
50. Liu, R.; Zhao, S.; Sun, S.; Cui, Y. Experimental study of the mechanical properties and microstructure of basalt fiber-reinforced concrete. *J. Mater. Civ. Eng.* **2023**, *35*, 04023205. [CrossRef]
51. Ren, G.; Gao, X.; Zhang, H. Utilization of hybrid sisal and steel fibers to improve elevated temperature resistance of ultra-high performance concrete. *Cem. Concr. Compos.* **2022**, *130*, 104555. [CrossRef]
52. Banthia, N.; Majdzadeh, F.; Wu, J.; Bindiganavile, V. Fiber synergy in Hybrid Fiber Reinforced Concrete (HyFRC) in flexure and direct shear. *Cem. Concr. Compos.* **2014**, *48*, 91–97. [CrossRef]
53. Naaman, A.E.; Wongtanakitcharoen, T.; Hauser, G. Influence of different fibers on plastic shrinkage cracking of concrete. *ACI Mater. J.* **2005**, *102*, 49–58. [CrossRef]
54. Wu, Z.; Shi, C.; Khayat, K.H. Investigation of mechanical properties and shrinkage of ultra-high performance concrete: Influence of steel fiber content and shape. *Compos. Part B Eng.* **2019**, *174*, 107021. [CrossRef]
55. Afroughsabet, V.; Teng, S. Experiments on drying shrinkage and creep of high performance hybrid-fiber-reinforced concrete. *Cem. Concr. Compos.* **2020**, *106*, 103481. [CrossRef]
56. Shen, Y.; Li, Q.; Huang, B.; Liu, X.; Xu, S. Effects of PVA fibers on microstructures and hydration products of cementitious composites with and without fly ash. *Constr. Build. Mater.* **2022**, *360*, 129533. [CrossRef]
57. Chen, Y.; Liu, P.; Sha, F.; Yu, Z.; He, S.; Xu, W.; Lv, M. Effects of Type and Content of Fibers, Water-to-Cement Ratio, and Cementitious Materials on the Shrinkage and Creep of Ultra-High Performance Concrete. *Polymers* **2022**, *14*, 1956. [CrossRef]
58. Mashrei, M.; Sultan, A.M.; Mahdi, A. Effects of polypropylene fibers on compressive and flexural strength of concrete material. *Int. J. Civ. Eng. Technol.* **2018**, *9*, 2208–2217.
59. Alhozaimy, A.M.; Soroushian, P.; Mirza, F. Mechanical properties of polypropylene fiber reinforced concrete and the effects of pozzolanic materials. *Cem. Concr. Compos.* **1996**, *18*, 85–92. [CrossRef]
60. Lee, J.-H. Influence of concrete strength combined with fiber content in the residual flexural strengths of fiber reinforced concrete. *Compos. Struct.* **2017**, *168*, 216–225. [CrossRef]
61. Qureshi, L.A.; Sheikh, M.I.; Sultan, T. Effect of Mixing Fiber Cocktail on Flexural Strength of Concrete. *Procedia Eng.* **2013**, *54*, 711–719. [CrossRef]
62. He, P.; Zhang, B.; Lu, J.-X.; Poon, C.S. A ternary optimization of alkali-activated cement mortars incorporating glass powder, slag and calcium aluminate cement. *Constr. Build. Mater.* **2020**, *240*, 117983. [CrossRef]
63. Shi, C.; Jiao, D.; Zhang, J.; Wang, D.; Zhang, Y.; Farzadnia, N.; Hu, X. Design of high performance concrete with multiple performance requirements for #2 Dongting Lake Bridge. *Constr. Build. Mater.* **2018**, *165*, 825–832. [CrossRef]
64. *T/CCES49-2024*; Standard for Design of Macro Fiber Reinforced Concrete Structures (In Chinese). China Architecture & Building Press: Beijing, China, 2024.
65. Li, Z.; Liu, X.; Sun, G. Pore structure of fiber-reinforced geopolymer recycled concrete: Effects on mechanical properties and drying shrinkage. *J. Build. Eng.* **2025**, *111*, 112990. [CrossRef]
66. Liu, Y.; Ren, Y.; Li, Q.; Shi, C. Influence of steel fiber hybridization on the static mechanical performance of ultra-high performance geopolymer concrete (UHPGC). *Cem. Concr. Compos.* **2025**, *160*, 106064. [CrossRef]

Disclaimer/Publisher's Note: The statements, opinions and data contained in all publications are solely those of the individual author(s) and contributor(s) and not of MDPI and/or the editor(s). MDPI and/or the editor(s) disclaim responsibility for any injury to people or property resulting from any ideas, methods, instructions or products referred to in the content.